Simultaneously enhanced transmission and artificial optical activity in gold film perforated with chiral hole array

Benfeng Bai,[1,2,3,][*] Janne Laukkanen,[1] Anni Lehmuskero,[1] and Jari Turunen[1]

[1]*Department of Physics and Mathematics, University of Eastern Finland (Joensuu Campus), P.O. Box 111, FI-80101 Joensuu, Finland*
[2]*State Key Laboratory of Precision Measurement Technology and Instruments, Department of Precision Instruments, Tsinghua University, Beijing 100084, China*
[3]*Tsinghua-Foxconn Nanotechnology Research Center, Tsinghua University, Beijing 100084, China*

We propose a simple two-dimensional metallic periodic chiral structure (PCS) consisting of a dielectric substrate and a thin gold film perforated with gammadion-shaped chiral hole array, in which the transmittance and artificial optical activity can be simultaneously enhanced. The principle and optical performance of the PCS are demonstrated through the experimental realization of a PCS sample, from numerical design, fabrication, to optical characterization. Good agreement between theory and experiment has been obtained. The PCS sample shows an enhanced transmittance of 53% at wavelength 1168 nm, accompanied nearby by a polarization rotation peak with the effective specific rotatory power up to 10^5 deg/mm. The enhancement mechanism of the dual effect is thoroughly studied by investigating the optical anomalies (i.e., Rayleigh anomalies, surface plasmon polaritons, and localized surface plasmons) in the PCS and their roles in the light-matter interaction. Several light-anomaly coupling regimes have been revealed. The single-layer metallic PCS is relatively easy to realize in optical frequencies by using mature microfabrication techniques such as electron-beam lithography and lift-off technique. The physical insight into the enhancement mechanism provides guidelines to develop more complicated PCS, such as multilayer PCS with metal and dielectric inclusions, which can produce stronger optical activity and better optical performance.

PACS number(s): 78.20.Ek, 73.20.Mf, 42.79.Dj, 42.25.Ja

I. INTRODUCTION

The artificially induced optical activity and circular dichroism in two-dimensional (2D) (Refs. 1–7) and three-dimensional (3D) (Refs. 8–13) periodic chiral structures (PCS) have been intensively studied in recent years. Such structures usually are composed of common optical materials (such as metals and dielectrics) without optical activity; however, due to their chiral structural features that resemble the molecular or crystalline chirality in natural chiral media (such as sucrose solution and quartz, respectively), optical activity can also be produced in PCS and may be further enhanced by various electromagnetic resonances. For example, giant polarization rotatory power (several orders larger than that in natural chiral media) (Refs. 1, 8, and 9) and tens-of-degree polarization rotation[6] have been observed in the zero-order transmission in some previously investigated PCS.

The PCS differ from traditional periodic polarizing elements such as wire grid polarizers[14,15] and film stacks[16] in the sense that the polarization conversion in PCS is realized via *circular form birefringence/dichroism* where left-circularly polarized (LCP) and right-circularly polarized (RCP) waves are eigenpolarizations of the structures;[17] in contrast, traditional grating polarizers[14–16] achieve the polarizing effect via *linear form birefringence* where two mutually orthogonal linearly polarized waves are eigenpolarizations. Owing to this new principle, the PCS have two distinct characteristics/advantages over traditional polarizing elements. First, unlike some linear grating polarizers that should work under *oblique* or *conical* illumination mountings,[18,19] the PCS can produce large polarization conversion under *normal* incidence.[17] Second, due to circular birefringence, the polarization conversion output in the PCS does not depend on the initial polarization direction of incident light, i.e., there is no need to align the incident polarization orientation in application. These characteristics are obviously more convenient and favorable from an application point of view. In addition, the PCS have some other peculiar polarizing properties, such as the reciprocity of the polarizing effect and no polarization conversion in reflection.[17] All of these features make PCS promising candidates to be developed as novel-type compact polarizing elements that can be used in, e.g., integrated electro-optic systems.

The light-matter interaction in PCS, from an effective-medium point of view, can be described by the classical constitutive equation of chiral media[20]

$$\mathbf{D} = \epsilon\mathbf{E} + i\xi\mathbf{k} \times \mathbf{E}, \qquad (1)$$

where ϵ is the unperturbed (achiral) permittivity tensor of the effective medium, $\mathbf{k}$ is the wave vector, and ξ is known as the gyratory coefficient. Therefore, to achieve large optical activity in PCS, an intuitive idea is to increase the gyratory coefficient ξ as much as possible by properly designing the PCS with high chirality. Extending 2D PCS to 3D or quasi-3D designs[8–13] is one such attempt. However, 3D PCS usually impose many challenges and difficulties to the fabrication process due to the increased structural complexity. This is why most 3D PCS realized so far work in microwave[8,13] and far infrared domain.[12] To reach visible and near-infrared domain, the period of PCS should be small enough compared with the corresponding operation wavelength. Therefore, it is always preferred if large optical ac-
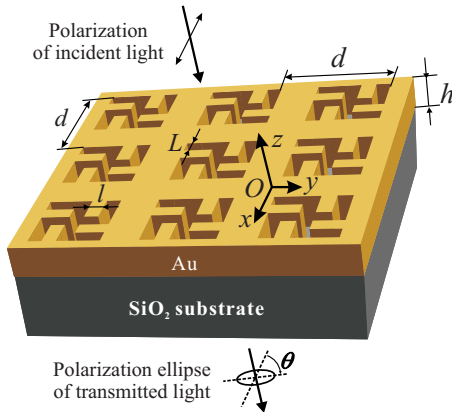
FIG. 1. (Color online) Geometry of the PCS with a gold film perforated with gammadion-shaped hole array on a fused silica substrate.

tivity can be achieved in simple 2D PCS, which can be manufactured relatively easily with mature microfabrication techniques such as electron-beam lithography.

In 2D PCS, although the maximization of chirality factor ξ is limited, the optical activity can nevertheless be enhanced by various optical resonances in *subwavelength* PCS (whose period d is comparable with or smaller than the wavelength λ). It has been revealed that surface-plasmon resonance (SPR) in metallic PCS (Refs. [1–5]) as well as the guided-mode resonance and Fabry-Pérot resonance in dielectric PCS (Ref. [7]) can contribute to the enhancement of optical activity. However, the large transmission loss in previous PCS is a major defect that dims their application prospect. Metallic PCS suffer from serious absorption at resonance due to the dissipation of energy in surface-plasmon polaritons (SPPs) (Refs. [1], [4], [8], and [13]) while dielectric PCS often get suppressed transmission at guided-mode resonance.[6,7] Therefore, it has been a vital issue and main objective in the development of PCS to produce simultaneously large optical activity and high transmittance.

The extraordinary transmission effect in perforated[21] or corrugated[22] metallic films has been well known for several years. Although there is still debate on the physical mechanism of enhancement,[23–26] it is commonly admitted that surface plasmons, including SPP Bloch waves on a periodic metal surface and localized surface plasmons (LSPs) excited in metallic particles or voids, play a crucial role in mediating the light transmission.[26] According to our previous study,[7,17] a key factor of producing large optical activity in PCS is to provide a channel for the incident light to be efficiently coupled to some surface or guided modes in the PCS, so that the LCP and RCP components may experience different coupling strength and phase change. Since both the extraordinary transmission and artificial optical activity may be related to surface plasmons, it is natural to consider synchronous realization of the two effects.

In this work, we propose a metallic PCS composed of a fused silica substrate covered by a gold film perforated with gammadion-shaped chiral hole array, as shown in Fig. 1. As an inductive structure, it is complementary compared with most previous 2D and quasi-3D metallic PCS

structures[1–5,8,9,13] that usually take the form of arrays of isolated chiral metal particles. Such particle type, or capacitive, PCS are not necessarily efficient geometries to excite and sustain propagating SPP modes for lack of connected metal surface. Although the LSPs on particles can be excited, they are less efficient than the propagating modes to accumulate phase difference between the LCP and RCP components during their propagation and, on the other hand, increase the dissipation of electromagnetic energy. Therefore, with the hole-type PCS, we expect to achieve the enhanced dual effect via the efficiently excited SPPs.

The paper is organized as follows. In Sec. II, we present the experimental realization of a hole-type PCS with simultaneously enhanced transmission and optical activity, from numerical design and fabrication to optical characterization. Then, in Sec. III, the enhancement mechanism of the dual effect is thoroughly studied by investigating the optical anomalies in the PCS as well as their interaction with the incident light. Several light-anomaly coupling regimes are revealed. In Sec. IV, the measures for optimizing the enhanced dual effect are discussed and the simulation results of an optimized case is demonstrated. Section V summarizes the work.

II. EXPERIMENTAL REALIZATION OF A PCS WITH DUAL EFFECT

A. Numerical design

The optical response of the PCS is rigorously simulated with the Fourier modal method (FMM) for crossed gratings with fourfold rotational (C_4) symmetry,[27] which is based on rigorous electromagnetic theory of gratings and is an optimization of the standard FMM (Ref. [28]) by using a group-theoretic approach.[29] The method first Fourier factorizes both the electromagnetic field and the periodic permittivity function of the grating media such that the Maxwell's equations are transformed into the discretized Fourier space; then by solving an eigenvalue problem in the grating layer and matching the boundary conditions at interfaces between different spatial regions, the fields inside and outside the modulated region can be readily solved. The reformulated FMM is specially developed for modeling C_4 symmetric crossed gratings with faster computation speed and better convergence, and is therefore most suitable for the study of our PCS.

A linearly polarized plane wave is assumed to illuminate the PCS at normal incidence with its polarization direction arbitrarily mounted. After the interaction with the PCS, the directly transmitted light (i.e., the zeroth diffraction order of the grating) usually becomes elliptically polarized. The polarization change is described by a polarization rotation angle θ (the angle between the major semiaxis of the polarization ellipse and the incident polarization direction, as shown in Fig. 1) and an ellipticity angle χ (which is defined by tan χ as the minor-to-major-axis ratio of the polarization ellipse).[30]

We choose gold as the metal film material for the efficient excitation of SPPs in optical frequencies. The gold refractive index used in simulation was measured by ellipsometry on a 100-nm-thick homemade gold film, as the refractive index of
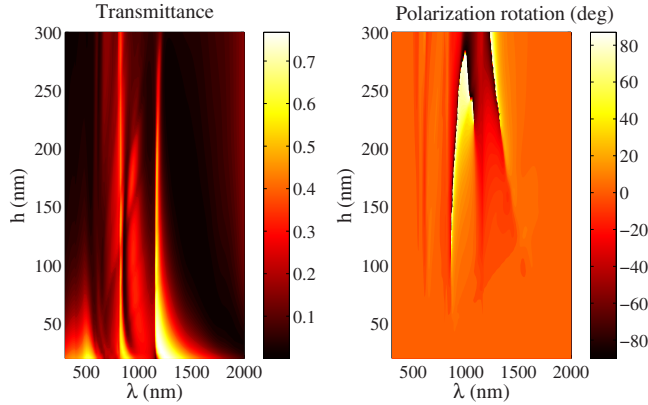
FIG. 2. (Color online) Numerically calculated transmittance and polarization rotation angle θ of the directly transmitted light in the PCS with respect to wavelength λ and film thickness h.

a thin metal film can be considerably different from that of bulk metal.[31] It is crucial for the generation of optical activity in 2D PCS that the cover and substrate materials are different.[17] Taking into account the feasibility of fabrication, we design the PCS with period $d=800$ nm and the gammadion dimensions $L=l=120$ nm. Then the only structural parameter to be optimized is the film thickness h.

Figure 2 shows the simulated transmittance and polarization rotation angle θ of the directly transmitted light with respect to the wavelength λ and film thickness h. It is seen that there are two main branches of polarization rotation maxima (one around wavelength 850 nm and the other around 1150 nm) corresponding to the vicinities of two transmittance maxima that should be attributed to the excitation of SPPs on the upper (air-gold) and lower (gold-silica) interfaces (the physical mechanism will be analyzed in detail in Sec. III). Furthermore, one can see that when the film thickness is beyond a certain limit (say, $h>80$ nm), tens-of-degree polarization rotation accompanied by an enhanced transmission over 50% may be realized in the PCS. This is a practical guideline to the fabrication.

B. Sample fabrication

We have fabricated our first samples by using electron-beam lithography and lift-off technique. First, a $1''$ fused silica wafer was spin coated with PMMA resist, which was then patterned with a Vistec EBPG5000+ES HR electron-beam patterning tool. After exposure, the resist was developed in methyl iso-butyl ketone:isopropanol 1:2 solution and rinsed in isopropanol. Then, after an adhesion layer of 3-nm-thick chromium was sputtered on the sample, an 80-nm-thick gold layer was deposited by thermal evaporation. Finally, the remaining resist as well as the metal on top of it was removed in acetone.

Due to the limitation of the lift-off technique, the maximum gold film thickness that we can achieve is around 80 nm. Figure 3 shows the scanning electron microscope (SEM) image of a fabricated PCS sample with left-twisted gammadion pattern, whose parameters are $d=800$ nm, $h=80$ nm, $L=108$ nm, and $l=127$ nm.

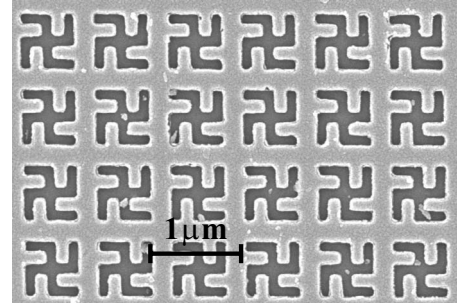FIG. 3. Top-view SEM image of a fabricated PCS sample.

C. Optical characterization

The optical properties of the PCS sample were characterized by ellipsometry. We employed a variable angle spectroscopic ellipsometer VASE produced by J. A. Woollam Co. to measure the transmittance and polarization state of the transmitted light under normal incidence in the wavelength range 300–1500 nm.

In the polarization measurement, the ellipsometer outputs ψ and δ that are defined by

$$\frac{t_p}{t_s} = \tan\psi \exp(i\delta), \tag{2}$$

where t_p and t_s are the complex transmission coefficients of two mutually orthogonal linearly polarized components. Note that the orientation of the s-p coordinate system can be arbitrary with respect to the Oxy system (with the x and y axes along the two periodic directions) due to the circular birefringence in the PCS, which simplifies the alignment of the sample. The above measurement actually corresponds to the case that a linearly polarized light is incident with its polarization direction parallel to the main diagonal of the s-p coordinate system. Therefore, the polarization rotation angle θ (with the clockwise rotation defined as the positive sense) of the transmitted light can be derived from[30]

$$\tan[2(45\,° - \theta)] = \tan 2\psi \cos\delta. \tag{3}$$

After the full dispersion spectrum of θ is obtained, the spectrum of the ellipticity angle χ can be easily calculated numerically by Kramers-Kronig transformation.[32,33]

Figure 4 shows the obtained measurement results of the transmittance and polarization spectra of the PCS sample, compared with the theoretical counterparts calculated with the practical structural parameters. We can see very good agreement between them. The small discrepancies are probably due to structure imperfections, surface roughness, and the uncertainty of the measured structural dimensions. Note that the abrupt change around $\lambda=1050$ nm in the measured transmittance curve is caused by the change in detectors in the ellipsometer; it is not a physical effect.

In the spectra there are two main transmission peaks around wavelengths 824 and 1168 nm, which are related to the excitation of SPPs on the air-gold and gold-silica interfaces, respectively (the detailed analysis is given in Sec. III). In the vicinity of each resonance, the polarization conversion effect (including the polarization rotation and elliptization) is
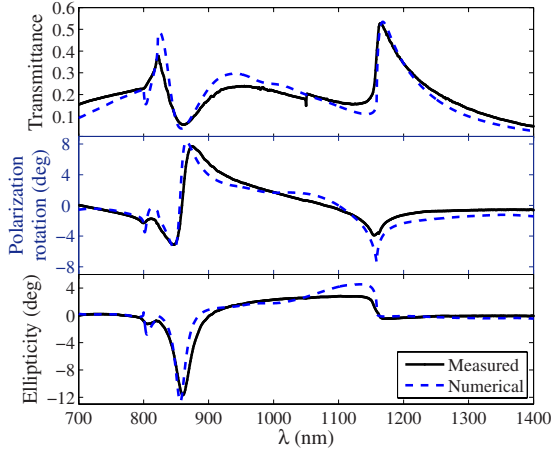
FIG. 4. (Color online) Experimentally measured and numerically calculated transmittance and polarization spectra of the PCS sample under normal incidence.
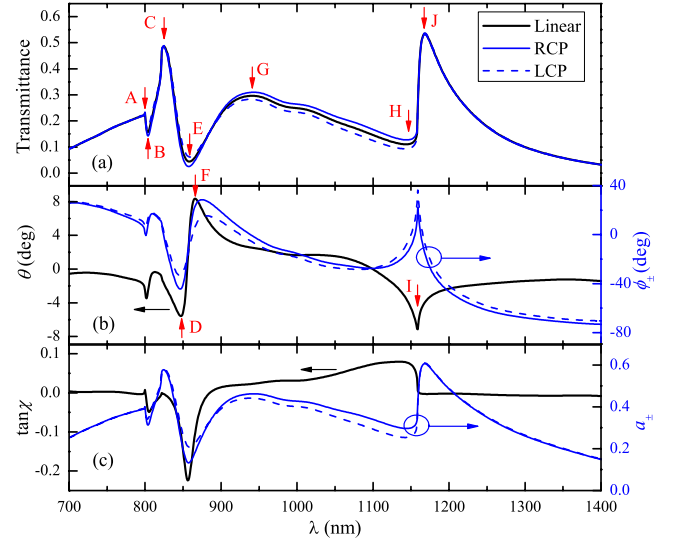

FIG. 5. (Color online) Calculated transmittance and polarization spectra of the PCS sample for the linearly polarized illuminating light as well as its LCP and RCP components. (a) Transmittance. (b) Polarization rotation angle θ and the phases $\phi_\pm$ of $t_\pm$. (c) Ellipticity $\tan \chi$ and the amplitudes $a_\pm$ of $t_\pm$. The vertical arrows with letters indicate several characteristic points on the spectra. The horizontal arrows in (b) and (c) indicate whether left or right scales should be considered.

enhanced likewise. Especially, around 1168 nm, a large polarization rotation (about 8° in theory and 4° in measurement) is observed nearby the transmittance peak of 53%, which is an unambiguous manifestation of the expected simultaneously enhanced dual effect. The corresponding *effective specific rotatory power* (i.e., the polarization rotation angle per unit thickness of the chiral film) reaches 10^5 deg/mm, which is one or two orders larger than that of previously reported particle-type 2D metallic PCS working in the visible and near-infrared spectral range[1,9] and is several orders larger than that of natural chiral media (such as quartz, cinnabar, and liquid crystals, whose specific rotatory power is 20 deg/mm, 600 deg/mm, and 10^3 deg/mm, respectively[34]). However, around wavelengths 847–866 nm the enhanced polarization rotation (whose peak value is about 8° in both theory and experiment) is shifted away from the spectral position of the transmission peak and corresponds to a transmittance minimum. This means that the enhanced polarization effect may be accompanied by either an *enhanced* or *suppressed* transmission. Therefore, the underlying physical mechanism must be thoroughly studied to reveal how to achieve and improve the simultaneously enhanced dual effect.

III. ENHANCEMENT MECHANISM

A. Circular birefringence in the PCS

To investigate the light-matter interaction in the PCS, we should first ascertain the eigenpolarizations of the proposed PCS under normal incidence. This can be done by using, e.g., Jones matrix calculus.[30] For directly transmitted light, the Jones vector describing its polarization state can be represented by the multiplication of a 2×2 Jones matrix (representing the polarizing component) and the Jones vector of the incident light,

$$\begin{pmatrix} E_x^{\text{out}} \\ E_y^{\text{out}} \end{pmatrix} = \begin{pmatrix} T_{11} & T_{12} \\ T_{21} & T_{22} \end{pmatrix} \begin{pmatrix} E_x^{\text{in}} \\ E_y^{\text{in}} \end{pmatrix}. \quad (4)$$

The number of independent elements of the Jones matrix is solely determined by the symmetry of the system (including

both the structure and the incident mounting). For the PCS with C_4 symmetry under normal incidence, symmetry considerations show that $T_{11}=T_{22}$ and $T_{12}=-T_{21}$. Therefore, the eigenvalues of the Jones matrix can be solved as $T_{11} \pm iT_{12}$ and the corresponding eigenvectors are $(1, \pm i)$, which represent the RCP and LCP waves. This means that the RCP and LCP waves go through the PCS with only the change in their phases and amplitudes (scaled by the eigenvalues) while the polarization states are maintained. Therefore, circular birefringence indeed takes place in the PCS.

If we define the complex transmission coefficients of the RCP (+) and LCP (−) waves as $t_\pm = a_\pm \exp(i\phi_\pm)$, then the polarization rotation angle θ and the ellipticity angle χ can be derived as

$$\theta = \frac{1}{2}(\phi_+ - \phi_-), \quad \tan \chi = \frac{a_+ - a_-}{a_+ + a_-}. \quad (5)$$

Henceforth, to study the generation and enhancement of the optical activity, it suffices to explore how the LCP and RCP waves are coupled to and interact with the optical modes in the PCS, during which the field amplitudes are changed and the phase difference is accumulated.

Since the numerical modeling reflects reality rather well, as seen from Fig. 4, we will perform the succedent investigation mainly by numerical simulation. Figure 5 shows the calculated spectra of the PCS sample under the illumination of a linearly polarized light as well as its LCP and RCP components. It is clearly seen from Figs. 5(b) and 5(c) that the circular birefringence relations given by Eq. (5) are well satisfied. In Fig. 5, we mark by vertical arrows and letters A–J several wavelengths of interest, where abnormal

changes (anomalies) are observed in both or either of the transmittance and polarization spectra. We proceed to analyze in detail the physical mechanisms behind these anomalies.

B. Optical anomalies in the metallic PCS

Optical anomalies in diffraction gratings, also known as Wood's anomalies, refer to rapid variations in the intensity spectra of various diffraction orders in certain narrow spectral bands. According to the classification by Hessel and Oliner,[35] there are two types of anomalies: *Rayleigh anomalies* (RAs), which often appear as abrupt turning points in spectra due to the onset or disappearance of particular diffraction orders, and *resonance anomalies*, which are smoother spectral variations and arise due to the excitation of certain surface or guided waves. The SPR in the metallic PCS is a resonance anomaly due to the excitation of SPP waves. Furthermore, according to Loewen and Popov,[36] there are the third-type anomalies, called *nonresonance anomalies*, which refer to the other nonresonant effects such as Littrow mounting zeros and Bragg anomalies. The LSPs in the gammadion holes of the metallic PCS can contribute to such anomalies because the LSPs can be excited in a wide spectral range without resonance (which will be shown later).

The metallic hole-type PCS can maintain all the above-mentioned three types of anomalies. Since the anomalies significantly affect the diffraction pattern, energy transportation, and field distribution in the PCS, we must distinguish these anomalies so as to identify different light coupling channels and regimes. Often anomalies of different types overlap with each other, making them difficult to distinguish, especially from the normal-incidence spectra where there are degeneracies of modes. Therefore, we should calculate the angle-resolved transmission spectra to lift up the mode degeneracy. In the following calculation, the incident direction of light is varied only in the Oxz plane with an incident angle α (the angle between the incident wave vector $\mathbf{k}^{in}$ and the z axis).

The condition for the occurrence of RA corresponding to the cutoff of the (p,q)th diffraction order is

$$\left|\mathbf{k}_\parallel^{in} + pK\hat{\mathbf{x}} + qK\hat{\mathbf{y}}\right| = nk_0, \qquad (6)$$

where $\mathbf{k}_\parallel^{in}$ is the projection of the incident wave vector on the Oxy plane, $K=2\pi/d$, $\hat{\mathbf{x}}$ and $\hat{\mathbf{y}}$ are unit vectors in the two periodic directions, $k_0=2\pi/\lambda$ is the wave number in vacuum, and n is the refractive index of the cover or substrate medium. For the case of incidence in the Oxz plane, Eq. (6) is specified as

$$\left(\frac{\sin \alpha}{\lambda} + \frac{p}{d}\right)^2 + \frac{q^2}{d^2} = \frac{n^2}{\lambda^2}. \qquad (7)$$

Similarly, by replacing the right-hand side of Eq. (6) with the modulus of the SPP wave vector on a *smooth* metal surface, we can obtain the approximate dispersion relation of the (p,q)th-order SPP Bloch wave excited on the *periodic* metal surface as
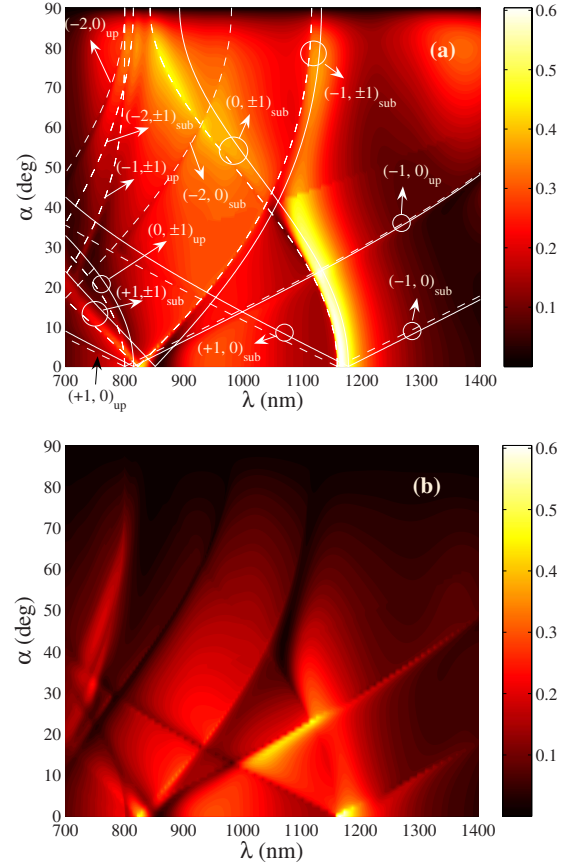

FIG. 6. (Color online) Calculated transmittance of the PCS sample with respect to the change of illumination wavelength λ and incident angle α for the (a) TM and (b) TE incident cases. The dashed and solid lines in (a) are the dispersion curves of RAs and SPP Bloch waves of various orders, calculated with Eqs. (7) and (8), respectively. Only the SPP modes with order indices $|p|,|q| \leq 1$ are demonstrated. The texts "up" and "sub" indicate the modes on the upper (air-gold) and substrate (gold-silica) interfaces, respectively.

$$\left(\frac{\sin \alpha}{\lambda} + \frac{p}{d}\right)^2 + \frac{q^2}{d^2} = \frac{1}{\lambda^2}\frac{\epsilon_m \epsilon_d}{\epsilon_m + \epsilon_d}, \qquad (8)$$

where ϵ_m and ϵ_d are the permittivities of the metal and the adjacent dielectric. Note that, while Eq. (7) is accurate and is independent on the metal, Eq. (8) is an approximate relation determined by both the metallic and dielectric properties. Thus Eq. (8) is valid only for slightly modulated metal surfaces and ignores the coupling of SPPs on the upper and lower interfaces of the thin metal film. Nevertheless, we can still use it as a reference to help identify the SPP modes.

Figure 6 shows the calculated transmittance spectra of the PCS sample with respect to the change in illumination wavelength λ and incident angle α. Two polarization cases are investigated: the TM case with the magnetic field vector of the incident wave perpendicular to the incident plane (i.e., the plane containing the incident wave vector and the grating normal) and the TE case with the electric field vector perpendicular to the incident plane. To help distinguish the anomalies, we also plot in Fig. 6(a) the dispersion curves of

RAs (dashed lines) and SPPs (solid lines) of various orders, which are calculated analytically with Eqs. (7) and (8), respectively. We can see clearly the signatures of *all* RAs in both the TM and TE cases, where the numerical and analytical RA traces are exactly superposed with each other. The SPP dispersion curves, though approximate, show qualitatively the spectral positions of the SPRs, which are always redshifted a bit with respect to the corresponding RAs.

The traces of SPP modes are not visible for all orders in the transmittance spectra. This is reasonable because only some low-order SPP Bloch modes can be efficiently excited on a metal grating surface,[26] which sometimes even lead to suppressed transmission.[23,25] In Fig. 6, at non-normal incidence, only one enhanced transmission peak is evident around wavelengths 1100–1170 nm in the TM case, which is related to the excitation of the $(0, \pm 1)_{\mathrm{sub}}$ SPP modes; at normal incidence, however, the SPP modes of same orders (propagating in different directions) degenerate, leading to stronger SPP excitation on both the upper and substrate interfaces around wavelengths 824 nm and 1168 nm, respectively. To exactly identify the SPPs (especially, to distinguish the cavity LSPs in the gammadion holes and the SPPs on the grating surface, both of which may contribute to the enhanced transmission), the far-field transmittance spectra are not sufficient. Thus the characteristic near-field distribution and energy flow must be inspected.

We have calculated the distribution of the electric field components $E_{\parallel} \equiv (E_x^2 + E_y^2)^{1/2}$ and E_z as well as the energy flow on both the upper (air-gold) and substrate (gold-silica) interfaces of the PCS sample at normal incidence. The planes of calculation were selected 20 nm above the respective interfaces in the dielectric side, so that the near-field features of SPPs can be best presented. The energy flow is obtained by calculating the time-averaged Poynting vector $\langle \mathbf{S} \rangle = \frac{1}{2} \mathrm{Re}(\mathbf{E} \times \mathbf{H}^*)$. Except for the RAs, we calculated at each wavelength of the interesting points indicated in Fig. 5(a) for RCP and LCP illuminations so as to intuitively observe the different light-anomaly interactions and to distinguish between the LSPs and SPPs.

As an example, Fig. 7 shows the near-field plots of the PCS under RCP and LCP illuminations at $\lambda = 1168$ nm corresponding to point J in Fig. 5(a). We can see unambiguously the following features. At the air-gold interface, the field is mostly localized in the gammadion holes with the $E_{\parallel}$ component dominant and the energy flowing longitudinally into the holes, showing the characteristics of cavity LSPs. Whereas, at the gold-silica interface, the field is primarily localized on the open continuous metal surface with the E_z component much stronger than the in-plane component $E_{\parallel}$; meanwhile, the $\langle \mathbf{S} \rangle$ vector has a dominant in-plane component, meaning that the energy flows along the metal surface in the xy plane. All of these reveal the presence of SPPs on the substrate interface. The energy flow forms vortices on the metal surface, as a result of the interference of the $\mathrm{SPP}_{\mathrm{sub}}^{(\pm 1,0)}$ and $\mathrm{SPP}_{\mathrm{sub}}^{(0,\pm 1)}$ modes. Therefore, we can conclude that at $\lambda = 1168$ nm there is a hybrid of SPPs and LSPs while the SPPs are dominant. This is consistent with the estimated SPP excitation wavelength $\lambda = 1178$ nm predicted according to Eq. (8) and the dispersion curve in Fig. 6.

Furthermore, by comparing the fields of RCP and LCP cases in Fig. 7, we can see that they have similar field fea-
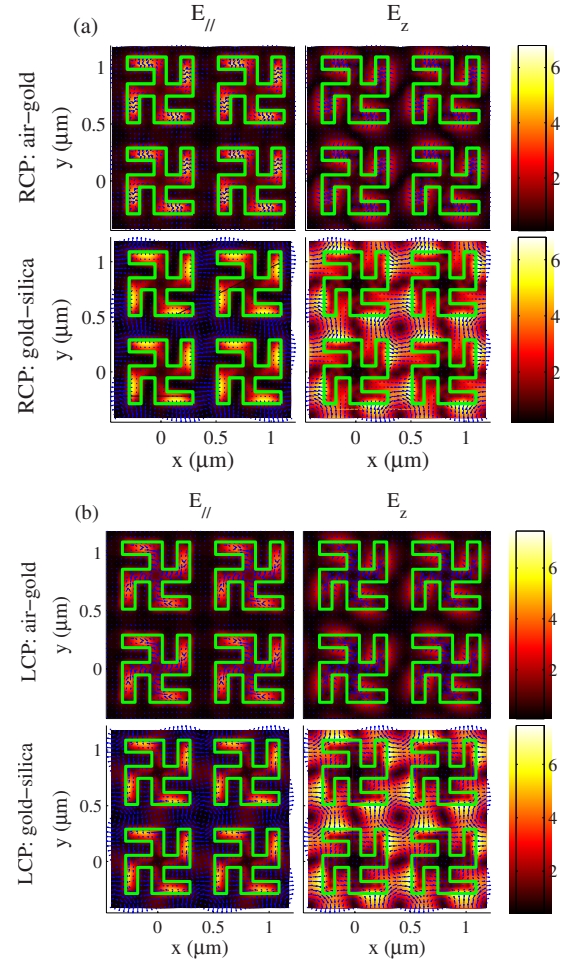

FIG. 7. (Color online) Distribution of the amplitudes of $E_{\parallel}$ and E_z (color plot, in the unit of the incident field amplitude) and the energy flow (arrows with the arrow length proportional to the magnitude of the time-averaged Poynting vector) on the air-gold and gold-silica interfaces under the normal incidence of (a) RCP and (b) LCP waves at $\lambda = 1168$ nm.

tures (field localization, energy flow, etc.), meaning that the dominant anomalies are the same. However, due to the different interactions of the RCP and LCP waves with the chiral structure, the anomalies affect the coupling of RCP and LCP waves differently, manifested in the energy flow and coupling strength. For example, under the RCP and LCP illuminations, the directions of energy flow vortices on the substrate interfaces are opposite and the enhancement factors of the E_z field amplitude are 6.80 and 7.45, respectively. These lead to the accumulated phase difference (circular birefringence) and/or amplitude difference (circular dichroism) of the RCP and LCP waves, as observed in Figs. 5(b) and 5(c).

Similarly, we can ascertain all the dominant anomalies at points A–J indicated in Fig. 5. Since at each wavelength the basic near-field features of the RCP and LCP cases are similar except for the energy flow direction and field coupling strengths, we show in Figs. 8–11 only the near-field distributions for the RCP incidence case at several typical wavelength points B (802 nm), C (824 nm), E (858 nm), and G (941 nm). At point B (Fig. 8), the SPP excitation on the air-gold surface is evident, corresponding to the $\mathrm{SPP}_{\mathrm{up}}^{(\pm 1,0)}$
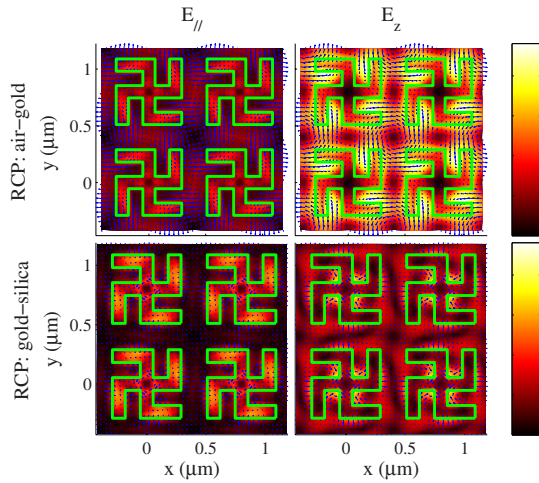
FIG. 8. (Color online) Similar to Fig. 7 but for RCP case at λ =802 nm.

FIG. 10. (Color online) Similar to Fig. 7 but for RCP case at λ =858 nm.

and $\text{SPP}_{\text{up}}^{(0,\pm1)}$ modes. At point C (Fig. 9), the cavity LSPs in gammadion holes are dominant, although the SPPs on the gold-silica interface are still present and couple with the LSPs. At point E (Fig. 10), the $\text{SPP}_{\text{sub}}^{(\pm1,\pm1)}$ modes are excited, whose interference pattern and energy flow are intrinsically different from those of the $(\pm1,0)$ and $(0,\pm1)$ order SPPs as shown in Fig. 7. At point G (Fig. 11), we can see that at both the air-gold and gold-silica interfaces the cavity LSPs are dominant, although the impact of SPPs does not totally disappear. In this way, we can characterize the dominant anomalies at all the indicated points, with the results summarized in Table I.

C. Light-anomaly coupling regimes

According to the far-field and near-field features summarized in Table I, we can uncover the light coupling characteristics in the PCS. First, all the RAs, SPPs, and LSPs can serve as efficient coupling channels for the RCP and LCP waves. The light coupling with SPPs and LSPs is intuitive
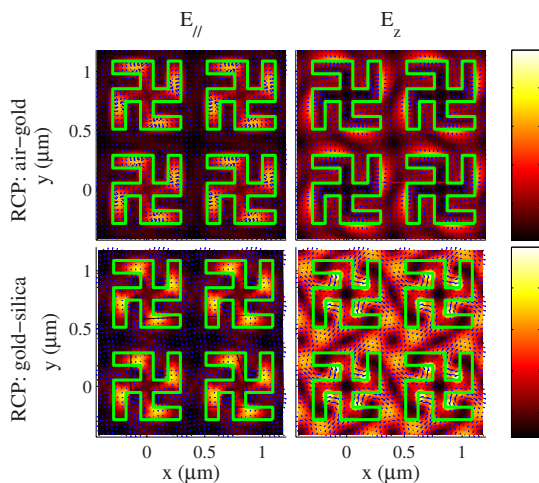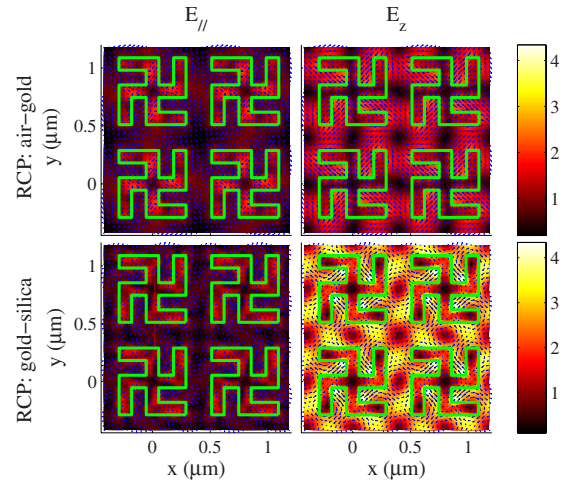
because SPPs and LSPs are localized surface waves or modes on the metal-dielectric interface which can exchange energy with the incident electromagnetic field. The RAs, though not any surface or guided modes, control the opening or closing of the diffraction channels of certain propagating orders, which lead to abrupt redistribution of electromagnetic energy in all other diffraction orders; thereby, the coupling performance of the incident light can still be significantly affected.

Second, the SPPs may lead to enhanced (at point J) as well as suppressed (at points B and E) transmission. However, they always contribute to the polarization effect positively. For example, at point B, the circular birefringence (and thereby the polarization rotation angle θ is maximized; at point E, the circular dichroism (and thereby the ellipticity χ) is maximized. At point J, although χ is locally minimized, it induces a θ peak nearby due to the fact that θ and χ obey the Kramers-Kronig relations. Also, thanks to the Kramers-Kronig relations, it is seen that the θ peak/zero usually corresponds to a χ zero/peak at strong resonances (see, e.g.,

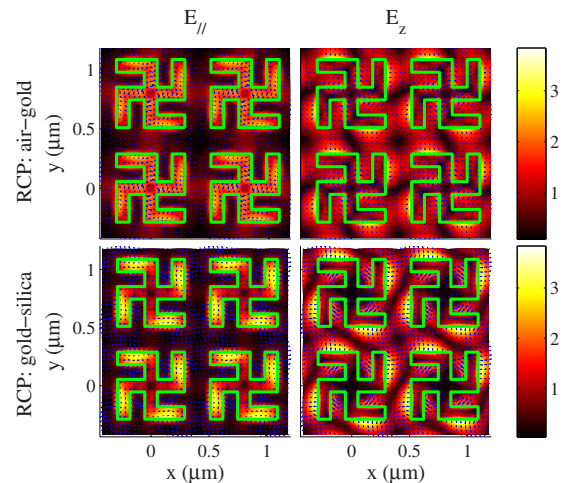FIG. 9. (Color online) Similar to Fig. 7 but for RCP case at λ =824 nm.

FIG. 11. (Color online) Similar to Fig. 7 but for RCP case at λ =941 nm.

TABLE I. Characteristics of the points indicated in the spectra of Fig. 5.

Point	λ (nm)	T (%)	θ (deg)	χ (deg)	Spectral feature[a]	Dominant anomalies[b]
A	800	23.0	−2.51	0.44	T peak, χ peak	$RA_{up}^{(\pm1,0)}$, $RA_{up}^{(0,\pm1)}$
B	802	16.5	−3.49	−1.39	T dip, θ peak	$SPP_{up}^{(\pm1,0)}$, $SPP_{up}^{(0,\pm1)}$
C	824	46.8	−1.01	0.00	T peak, χ zero	$RA_{sub}^{(\pm1,\pm1)}$, $LSP+SPP_{sub}$
D	847	11.5	−5.59	−5.94	θ peak	$LSP+SPP_{sub}$
E	858	4.5	0.00	−12.27	T dip, θ zero, χ peak	$SPP_{sub}^{(\pm1,\pm1)}$
F	866	6.2	8.35	−5.79	θ peak	$LSP+SPP_{sub}$
G	941	29.6	2.54	1.31	T peak	$LSP+SPP_{sub}$
H	1143	11.0	−3.43	4.48	T dip	$LSP+SPP_{sub}$
I	1159	41.8	−7.83	0.29	θ peak	$RA_{sub}^{(\pm1,0)}$, $RA_{sub}^{(0,\pm1)}$
J	1168	53.5	−3.97	−0.16	T peak, χ zero	$SPP_{sub}^{(\pm1,0)}$, $SPP_{sub}^{(0,\pm1)}$

[a]The peaks of θ and χ refer to the maxima of the absolute values.
[b]Subscript—interface; superscript—order index.

points E and I in Fig. 5). This is a useful property of the PCS for their application as polarization control devices.

Third, in the full spectral range of interest (700–1400 nm), the hybridization or overlapping of RAs, SPPs, and LSPs commonly exists. Especially, at wavelengths between points B and J (where the first-order SPP_{up} and SPP_{sub} modes are excited, respectively), the LSPs are tightly combined with SPPs, which causes stronger circular birefringence/dichroism (see Fig. 5). At point C, the LSPs overlap with $RA_{sub}^{(\pm1,\pm1)}$, where the $(\pm1,\pm1)$ orders in the substrate side are on cutoff (turning from propagating to evanescent or vice versa); the grazing waves also strengthen the SPPs on the lower interface, leading to enhanced transmission. Therefore, we can say that the hybridization of anomalies is advantageous to the light coupling and benefits the enhanced transmission as well as the circular birefringence. This is consistent with the observations by McMahon *et al.*[37] on a thin gold film perforated with a square array of nanoholes.[38]

Finally, the roles and characteristics of the RAs, SPPs, and LSPs are different in modifying the optical response of PCS. SPPs are efficient light coupling channels for the RCP and LCP components to accumulate phase and amplitude differences, due to the relatively long propagation/interaction length of the SPPs. Also, since the SPPs can be excited in the vicinity of the resonance wavelength, the SPR peaks usually exhibit broadband and smooth features (see, e.g., the Fano-type feature at point J). Therefore, the impact of SPPs on the polarization effect is the most significant in all the three types of anomalies. In contrast, the RAs usually cause abrupt changes in spectra with sharp and narrow resonance features; their influence on the polarization effect is moderate unless a RA is hybridized with the SPPs (e.g., at point I). The LSPs are excited in a wide spectral range without any resonance condition. Though not contributing directly to the polarization effect, the LSPs provide an efficient channel for the tunneling of energy through the metallic film and mediate the coupling of anomalies on the upper and substrate interfaces.

Having recognized the characteristics of the anomalies, we can conclude several different coupling regimes in the PCS, through which the RCP and LCP components interact with the anomalies in the chiral structure and receive different modifications: (1) incident light→coupling to RAs and/or SPPs on the first interface→tunneling through LSPs →outcoupling to transmitted light. Examples: points A and B. (2) Incident light→tunneling through LSPs→coupling to RAs and/or SPPs on the second interface→outcoupling to transmitted light. Examples: points C, G, H, I, and J. (3) Incident light→coupling to RAs and/or SPPs on the first interface→tunneling through LSPs→coupling to RAs and/or SPPs on the second interface→outcoupling to transmitted light. Examples: points D, E, and F. (4) Incident light→tunneling through LSPs→outcoupling to transmitted light. Examples: the other nonresonant wavelengths, e.g., λ < 750 nm or > 1200 nm.

Among all the four regimes, only the first three can significantly change the transmission and polarization properties of the PCS because of the occurrence of RAs and/or SPPs. Especially, when there is coupling between the RAs and/or SPPs on the upper and substrate interfaces, i.e., regime (3), the resonance is the strongest.

IV. DISCUSSION AND PERSPECTIVE

From the investigation presented above, we have understood the mechanism of light-matter interaction in the 2D metallic PCS. Then a natural expectation is: how to optimize the PCS so as to realize stronger simultaneously enhanced dual effect? We may find some clues from the light coupling regimes.

First, the SPPs have been revealed as the most important anomalies for enhancing the polarization effect in the 2D metallic PCS. However, in our PCS they only enhance transmission in the *nondiffraction regime* (where there are only the directly transmitted and reflected zeroth orders, such as point J) while suppress it in the *diffraction regime* (where there exist higher diffraction orders, such as points B and E). This fact has also been more or less observed in some previous plasmonic structures with perforated metal films.[24–26,37,38] Although this is just an empirical observation, it shows that the opening of more diffraction channels may

affect the interaction of incident light with the SPPs as well as the reradiation of electromagnetic energy into the zeroth transmitted order. Therefore, we should mainly utilize the excitation of the $SPP_{sub}^{(\pm 1,0)}$ and $SPP_{sub}^{(0,\pm 1)}$ modes to get the simultaneously enhanced dual effect, i.e., the PCS should work in subwavelength regime.

Second, the hybridization of RAs and SPPs can significantly enhance transmission[37,38] as well as the polarization effect (see Fig. 5). Therefore, in the design of the PCS, one may try to realize the first-order RAs and SPPs (i.e., points I and J) as close as possible to each other, preferably overlapped.

Third, the important role of SPPs implies that the continuous metal surface is indeed necessary in the PCS to maintain propagating surface waves with which the RCP and LCP components of the incident wave can couple and interact efficiently. The chiral holes are also necessary to maintain the cavity LSPs that act as tunneling channels for transferring electromagnetic energy between the upper and substrate interfaces. In this sense, the hole-type 2D metallic PCS are indeed advantageous over the particle-type ones.

The above discussion provides some guidelines to the design of 2D metallic PCS. However, we should emphasize that, since in the thin-film PCS the overlapping and coupling of different anomalies are very common, it is rather difficult to figure out the contribution of each single anomaly. Therefore, in the design of other PCS, the interaction between different anomalies should also be analyzed specifically to characterize the device performance. Rigorous numerical modeling of the far-field and near-field responses of the PCS has been shown to be a useful and convenient tool to achieve this goal.

Before the end of the discussion, we want to show how the dual effect of the 2D metallic PCS can be improved by simply increasing the gold film thickness. It has been shown by numerical optimization in Fig. 2 that, if the gold film thickness h is large enough, tens-of-degree polarization rotation may be achieved. In Fig. 12, we calculated the transmittance and polarization spectra of a PCS with $d = 800$ nm, $L = l = 120$ nm, and $h = 200$ nm. Evidently, in this case the enhancement of the polarization effect is much stronger, especially in the spectral range between points B and J (still with the labeling in Fig. 5) where strongly hybridized LSPs and SPPs are dominant. For example, at point E where the $SPP_{sub}^{(\pm 1,\pm 1)}$ modes are excited, a suppressed transmission still occurs and the transmitted light is almost pure LCP due to the strong circular dichroism, meaning that the PCS can function as a LCP polarizer at this wavelength. In the vicinity of points I and J where the first-order SPPs and RAs are present, we observe a transmission peak of 34% accompanied by a peak polarization rotation up to $-32°$ with almost zero ellipticity ($\tan \chi = 0.05$), meaning that the PCS can work as a pure linear polarization rotator without elliptization at this wavelength.

With this example, we show the potential of the single-layer hole-type 2D metallic PCS. The experimental realization of such PCS with thicker gold film and high quality, however, needs fabrication methods other than the lift-off technique, which are under our investigation.
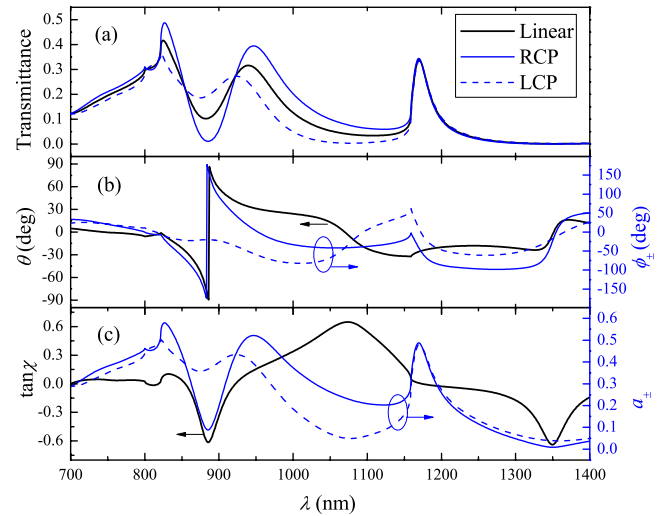

FIG. 12. (Color online) Similar as Fig. 5 but for a hole-type metallic PCS with $d = 800$ nm, $L = l = 120$ nm, and $h = 200$ nm.

V. CONCLUSIONS

In this work, we propose a design of 2D metallic PCS consisting of a fused silica substrate and a thin gold film perforated with gammadion-shaped chiral holes. The hole-type metallic PCS are advantageous over previous particle-type ones in the sense that they can produce simultaneously enhanced transmission and artificial optical activity, thanks to the excitation of SPPs and RAs on the upper and substrate interfaces of the grating and the cavity LSPs in the gammadion holes. These anomalies can couple and interact strongly with the incident light and mediate the different penetration of RCP and LCP components through the chiral film, leading to enhanced circular birefringence and dichroism. The increased transmittance in the hole-type PCS provides a solution to the serious transmission loss in previous metallic PCS. Furthermore, the single-layer 2D metallic PCS are easier to realize in optical frequencies, by using mature microfabrication techniques such as EBL and lift-off, compared with the more complicated 3D and quasi-3D PCS.

The principle and optical performance of the proposed PCS are demonstrated by the experimental realization of a PCS sample, from numerical design, fabrication, to optical characterization. Good agreement between theory and experiment has been obtained. An enhanced transmittance peak of 53% is observed at wavelength 1168 nm accompanied nearby by a polarization rotation peak (about 8° in theory and 4° in experiment) at normal incidence. The effective specific rotatory power reaches 10^5 deg/mm, which is one or two orders of magnitude larger than that of previous particle-type 2D metallic PCS and several orders larger than that of natural chiral media.

The underlying physical mechanism of the enhanced dual effect is thoroughly studied by investigating the optical anomalies (RAs, SPPs, and LSPs) in the PCS and their roles in the light-matter interaction. Several light-anomaly coupling regimes have been revealed. It is seen that the SPPs can significantly change the amplitudes and accumulate phase difference of the RCP and LCP waves, leading to en-

hanced optical activity; the RAs also cause polarization change, which is more remarkable if hybridized with the SPPs; the LSPs, though do not contribute to the optical activity directly, function as efficient channels of transferring and coupling energy between the two sides of the chiral metal film.

The physical insight into the enhanced dual effect provides us useful guidelines for the design and optimization of the 2D metallic PCS. Knowing the enhancement mechanism, we may develop more complicated PCS, such as multilayer PCS with both metal and dielectric inclusions, with which to produce stronger optical activity and better optical performance. The perspective is to develop PCS-based functional polarization elements used in, e.g., integrated electro-optic systems.

*Corresponding author; baibenfeng@tsinghua.edu.cn

[1] M. Kuwata-Gonokami, N. Saito, Y. Ino, M. Kauranen, K. Jefimovs, T. Vallius, J. Turunen, and Y. Svirko, Phys. Rev. Lett. **95**, 227401 (2005).

[2] K. Konishi, T. Sugimoto, B. Bai, Y. Svirko, and M. Kuwata-Gonokami, Opt. Express **15**, 9575 (2007).

[3] A. Papakostas, A. Potts, D. M. Bagnall, S. L. Prosvirnin, H. J. Coles, and N. I. Zheludev, Phys. Rev. Lett. **90**, 107404 (2003).

[4] M. Decker, M. W. Klein, M. Wegener, and S. Linden, Opt. Lett. **32**, 856 (2007).

[5] V. A. Fedotov, A. S. Schwanecke, N. I. Zheludev, V. V. Khardikov, and S. L. Prosvirnin, Nano Lett. **7**, 1996 (2007).

[6] X. Meng, B. Bai, P. Karvinen, K. Konishi, J. Turunen, Y. Svirko, and M. Kuwata-Gonokami, Thin Solid Films **516**, 8745 (2008).

[7] B. Bai, K. Konishi, X. Meng, P. Karvinen, A. Lehmuskero, M. Kuwata-Gonokami, Y. Svirko, and J. Turunen, Opt. Express **17**, 688 (2009).

[8] A. V. Rogacheva, V. A. Fedotov, A. S. Schwanecke, and N. I. Zheludev, Phys. Rev. Lett. **97**, 177401 (2006).

[9] E. Plum, V. A. Fedotov, A. S. Schwanecke, N. I. Zheludev, and Y. Chen, Appl. Phys. Lett. **90**, 223113 (2007).

[10] J. C. W. Lee and C. T. Chan, Opt. Express **13**, 8083 (2005).

[11] M. Thiel, G. von Freymann, and M. Wegener, Opt. Lett. **32**, 2547 (2007).

[12] J. K. Gansel, M. Thiel, M. Wegener, K. Bade, V. Saile, G. von Freymann, and S. Linden, in *Proceedings of the Conference on Lasers and Electro-Optics/International Quantum Electronics Conference*, OSA Technical Digest (Optical Society of America, Baltimore, MD, 2009).

[13] E. Plum, J. Zhou, J. Dong, V. A. Fedotov, T. Koschny, C. M. Soukoulis, and N. I. Zheludev, Phys. Rev. B **79**, 035407 (2009).

[14] T. Clausnitzer, H.-J. Fuchs, E.-B. Kley, A. Tuennermann, and U. Zeitner, in *Lithographic and Micromachining Techniques for Optical Component Fabrication II*, Proceedings of SPIE Vol. 5183, edited by E.-B. Kley and H. P. Herzig (SPIE, Bellingham, WA, 2003), p. 8.

[15] L. Chen, J. J. Wang, F. Walters, X. Deng, M. Buonanno, S. Tai, and X. Liu, Appl. Phys. Lett. **90**, 063111 (2007).

[16] I. Hodgkinson and Q. H. Wu, Appl. Phys. Lett. **74**, 1794 (1999).

[17] B. Bai, Y. Svirko, J. Turunen, and T. Vallius, Phys. Rev. A **76**, 023811 (2007).

[18] S. J. Elston, G. P. Bryan-Brown, and J. R. Sambles, Phys. Rev. B **44**, 6393 (1991).

[19] A. V. Kats and I. S. Spevak, Phys. Rev. B **65**, 195406 (2002).

[20] A. Yariv and P. Yeh, *Optical Waves in Crystals* (Wiley, New York, 1983).

[21] T. W. Ebbesen, H. J. Lezec, H. F. Ghaemi, T. Thio, and P. A. Wolff, Nature (London) **391**, 667 (1998).

[22] S. Wedge, I. R. Hooper, I. Sage, and W. L. Barnes, Phys. Rev. B **69**, 245418 (2004).

[23] Q. Cao and P. Lalanne, Phys. Rev. Lett. **88**, 057403 (2002).

[24] W. L. Barnes, W. A. Murray, J. Dintinger, E. Devaux, and T. W. Ebbesen, Phys. Rev. Lett. **92**, 107401 (2004).

[25] C. P. Huang, Q. J. Wang, and Y. Y. Zhu, Phys. Rev. B **75**, 245421 (2007).

[26] A. V. Zayats and I. I. Smolyaninov, J. Opt. A, Pure Appl. Opt. **5**, S16 (2003).

[27] B. Bai and L. Li, J. Opt. A, Pure Appl. Opt. **7**, 783 (2005).

[28] L. Li, J. Opt. Soc. Am. A Opt. Image Sci. Vis. **14**, 2758 (1997).

[29] B. Bai and L. Li, J. Opt. Soc. Am. A Opt. Image Sci Vis. **21**, 1886 (2004).

[30] E. Collett, *Polarized Light: Fundamentals and Applications* (Marker Dekker, New York, 1993).

[31] A. Lehmuskero, M. Kuittinen, and P. Vahimaa, Opt. Express **15**, 10744 (2007).

[32] H. Eyring, H. Liu, and D. Caldwell, Chem. Rev. **68**, 525 (1968).

[33] V. Lucarini, J. J. Saarinen, K.-E. Peiponen, and E. M. Vartiainen, *Kramers-Kronig Relations in Optical Materials Research* (Springer, Heidelberg, 2005).

[34] P. G. de Gennes, *The Physics of Liquid Crystals* (Clarendon, Oxford, 1974).

[35] A. Hessel and A. A. Oliner, Appl. Opt. **4**, 1275 (1965).

[36] E. G. Loewen and E. Popov, *Diffraction Gratings and Applications* (Marcel Dekker, New York, 1997).

[37] J. M. McMahon, J. Henzie, T. W. Odom, G. C. Schatz, and S. K. Gray, Opt. Express **15**, 18119 (2007).

[38] H. Gao, J. M. McMahon, M. H. Lee, J. Henzie, S. K. Gray, G. C. Schatz, and T. W. Odom, Opt. Express **17**, 2334 (2009).